Electronic Supplementary Information for

The proximity of the G-quadruplex to hemin impacts the intrinsic DNAzyme activity in mitochondria

Jiayu Zhang,‡[a] Xiaofang Song,‡[ab] Miaoren Xia,‡[a] Yanan Xue,[b] Mengxue Zhou,[a] Lifo Ruan,[a] Huiru Lu,[a] Jun Chen,*[a] Dongqi Wang,*[ac] Zhifang Chai[a] and Yi Hu*[a]

[a]CAS Key Laboratory for Biomedical Effects of Nanomaterials and Nanosafety, Multi-disciplinary Research Division, Institute of High Energy Physics and University of Chinese Academy of Sciences (UCAS), Chinese Academy of Sciences (CAS), Beijing 100049, P. R. China.

[b]Key Laboratory for Green Chemical Process of Ministry of Education, Hubei Key Laboratory for Novel Reactor and Green Chemistry Technology, Hubei Engineering Research Center for Advanced Fine Chemicals and School of Chemical Engineering and Pharmacy, Wuhan Institute of Technology, Wuhan 430205, P. R. China.

[c]State Key Laboratory of Fine Chemicals, Liaoning Key Laboratory for Catalytic Conversion of Carbon Resources, School of Chemical Engineering, Dalian University of Technology, Dalian 116024, P. R. China.

‡These authors contributed equally to this work.

Experimental Procedures

Materials

N,*N*′-Methylenebis(acrylamide), *N*,*N*-Dimethyldipropylenetriamine, (4-Carboxybutyl)triphenylphosphonium bromide (TPP) and 3-(4,5-Dimethyl-2-thiazolyl)-2,5-diphenyl-2H-tetrazolium bromide (MTT) were obtained from Sigma-Aldrich (Shanghai, China). *N*-(3-Dimethylaminopropyl)-*N*′-ethylcarbodiimide hydrochloride (EDC), *N*-hydroxysuccinimide (NHS), 3,3′,5,5′-Tetramethylbenzidine (TMB) were purchased from Aladdin (Shanghai, China). Hemin was purchased from Ark Pharm (USA). Fetal bovine serum (FBS) was purchased from PAN Biotech (Germany). Dulbecco's Modified Eagle Medium (DMEM) and penicillin/streptomycin solution were purchased from Hyclone (USA). Hoechst 33342 and MitoTracker Green were obtained from Life Technologies (Shanghai, China). MitoSOX Red Mitochondrial Superoxide Indicator was purchased from Yeasen Biotechnology (Shanghai, China). Cyanine-5 (Cy5) NHS ester was obtained from Lumiprobe (USA). GelStain was purchased from TransGen Biotech (Beijing, China). Hemin-G4-1 (5'-hemin-GGGAAAGGGAAAGGGAAAGGG-3') and Hemin-G4-2 (5'-hemin-GGGTAGGGCGGGTTGGGA-3') were obtained from Takara (Dalian, China). G4-1 (5'-GGGAAAGGGAAAGGGAAAGGG-3') and G4-2 (5'-GGGTAGGGCGGGTTGGGA-3') were synthesized by Sangon (Shanghai, China). All chemicals were analytical grade and used without further purification unless otherwise noted. The deionized water was used in the experiments.

Preparation of DNAzymes

DNAzymes were prepared as previously described with minor modifications.[1] Hemin-G4-1 or Hemin-G4-2 was dissolved in 10 mM Tris-HCl buffer (pH 7.4) containing 50 mM KCl at a final concentration of 8 μM and heated up to 95 °C, followed by cooling to room temperature. Hemin/G4-1 and Hemin/G4-2 were prepared as follows. 10 μM G4-1 or G4-2 was heated up to 95 °C in 10 mM Tris-HCl buffer (pH 7.4) containing

50 mM KCl and cooled down to room temperature. A final concentration of 8 μM hemin was incubated with the same concentration of G4-1 or G4-2 for 30 min.

Circular dichroism (CD)

Final concentration of 4 μM DNAzymes was prepared in $LiAsO_2(CH_3)_2$ buffer (pH 7.0) containing 50 mM KCl and 40% (W/V) PEG 200.[2] CD spectra were recorded on Circular Dichroism Spectrometer (Applied Photophysics, United Kingdom) with a 0.5 mm path length cuvette at room temperature.

***In vitro* analysis of the DNAzyme activity**

TMB powder was dissolved in DMSO at a concentration of 1 mg/mL. TMB working solution was prepared as follows. 9.06 mL C-C buffer (pH 6.4) containing 0.1 M citrate, 0.1 M sodium citrate and 20 mM KCl was mixed with freshly prepared 270 μL TMB (1 mg/mL) and 30 μL 0.75% (v/v) H_2O_2.[3] 20 μL of DNAzyme was mixed with 180 μL TMB working solution. The absorbance was recorded at 650 nm on a multimode microplate reader (Infinite M200 PRO, Tecan). V(ΔAbs/min) indicates the increase in absorbance relative to the time interval. The initial activity (V_0) was calculated with the absorbance versus reaction time (3 min) and ε value of TMB (39 000 M^{-1} cm^{-1}).[4]

Synthesis and characterization of TPP-conjugated polyamidoamines

TPP-conjugated polyamidoamines (TPAA) was prepared with Michael-addition type polymerization according to previous studies.[5, 6] Briefly, *N*,*N*′-Methylenebis(acrylamide) (0.311 g, 2.0 mmol) and *N*,*N*-Dimethyldipropylenetriamine (0.322 g, 2.0 mmol) were dissolved in methanol/water (v/v, 1:1) solution. The mixture was stirred at 55 °C for three days and then at room temperature for another 24 h after

adding EDC/NHS-activated TPP (0.289 g, 0.65 mmol). TPAA polymers were obtained by lyophilization after extensive dialysis against deionized water at pH 3 (adjusted by addition of HCl) and final dialysis against deionized water. The yield was ~31%. The chemical structure of TPAA polymer was characterized by ^{1}H NMR. ^{1}H NMR (D_2O): δ=1.55-1.85 (P-$CH_2C\boldsymbol{H}_2C\boldsymbol{H}_2$-), δ=2.00-2.20 (-$C\boldsymbol{H}_2CH_2N(CH_3)_2$ and -$NCH_2C\boldsymbol{H}_2CH_2N$-), δ=2.40-2.50 (P-$CH_2CH_2CH_2C\boldsymbol{H}_2CO$-), δ=2.50-2.70 (-$NCH_2C\boldsymbol{H}_2CONH$-, and P-$C\boldsymbol{H}_2CH_2CH_2$-), δ=2.75-2.85 (-$N(C\boldsymbol{H}_3)_2$), δ=3.00-3.20 (-$CH_2$(-$CH_2$-)$NC\boldsymbol{H}_2CH_2C\boldsymbol{H}_2N(CH_3)_2$, and -$CH_2$(-$CH_2$-)$NC\boldsymbol{H}_2CH_2CH_2N$-), δ=3.20-3.25 (-(-CO)$NC\boldsymbol{H}_2CH_2CH_2N$-, -$NHC\boldsymbol{H}_2CH_2CH_2N$(-$CH_2$-)$CH_2$-), δ=3.25-3.40 (-(-CO)$NC\boldsymbol{H}_2CH_2CONH$-, -$CH_2$(-$CH_2$-)$NC\boldsymbol{H}_2CH_2CONH$-), δ=3.55 (-$NHC\boldsymbol{H}_2CH_2CONH$-), δ=4.30-4.50 (-CONH-$C\boldsymbol{H}_2$-NHCO-), δ=7.55-7.75 (C$\boldsymbol{H}$ in benzene).

Preparation and characterization of TPAA/DNAzymes

TPAA/DNAzymes were prepared through the electrostatic interactions.[6] Briefly, TPAA and DNAzymes (or G-quadruplex) were dissolved in sodium acetate buffer (30 mM, pH 5.0), mixed and vortexed for 5 s, followed by incubation at room temperature for 30 min. Zeta potentials of TPAA, DNA (G4-1), TPAA/DNA (G4-1) were measured by Malvern Zetasizer Nano ZS90. The electrophoretic mobility shift assay (EMSA) was conducted as follows. Briefly, TPAA/DNA (G4-1) polyplexes with the N/P ratios of 5/1, 10/1, and 20/1 in sodium acetate buffer (30 mM, pH 5.0) were resolved on 1.5% agarose gel at 120 V in 1X TAE buffer for 60 min. The images were recorded with ChemiDoc MP (Bio-rad).

The nucleic acid dye displacement assay

DNA or DNAzymes were incubated with GelStain in 10 mM Tris-HCl buffer containing 50 mM KCl, and TPAA was then added with the N/P ratios of 0.2/1, 1/1,

5/1, 10/1, 20/1. Fluorescence was recorded on a multimode microplate reader (Infinite M200 PRO, Tecan) with excitation wavelength at 260 nm and emission at 600 nm before or after TPAA addition.[7] F_0 and F_N were the fluorescence before and after TPAA addition, respectively.

Cell culture

HeLa cells were cultured in DMEM supplemented with 10% FBS, 100 U/mL penicillin and 100 μg/mL streptomycin at 37 °C with 5% CO_2.

Mitochondrial targeting

Cyanine-5 NHS ester was conjugated to TPAA for imaging. After being incubated with Cy5-labeled TPAA or Cy5-labeled TPAA/DNAzymes, HeLa cells were stained with MitoTracker Green and Hoechst 33342. The images were recorded with confocal laser scanning microscopy (A1/LSM, Nikon). Pearson's correlation coefficient for colocalization was obtained by ImageJ.

Mitochondrial superoxide in HeLa cells

Briefly, HeLa cells were cultured to 70-80% confluence and incubated with fresh medium containing DNAzymes encapsulated by 20 μg/mL TPAA with the N/P ratio of 10/1 at 37 °C for 2 or 6 h. Afterward, a final concentration of 5 μM MitoSOX Red Mitochondrial Superoxide Indicator was added and incubated with the cells at 37 °C for 10 min. The cells were then washed with PBS for three times and stained with Hoechst 33342 (5 μg/mL) for another 15 min. The fluorescence was recorded with confocal laser scanning microscopy (A1/LSM, Nikon). Mitochondrial superoxide levels were analyzed by quantifying the fluorescence of MitoSOX with ImageJ.[8]

Cytotoxicity

The cytotoxicity of HeLa cells was estimated by MTT assay according to the manufacturer's instructions. HeLa cells were seeded into a 96-well plate with a density of 7000 cells/well and cultured at 37 °C with 5% CO_2 for 12 h. Increasing concentrations of TPAA from 0 to 500 μg/mL were added and incubated with the cells for 24 h to assess the cytotoxicity of TPAA. 0.36 μM DNAzymes encapsulated by TPAA (N/P = 10/1) were added and incubated with the cells for 2 or 6 h to detect the cytotoxicity of DNAzymes. A final concentration of 500 μg/mL MTT was added to each well and incubated for another 4 h at 37 °C. Solubilization solution was added to dissolve the formazan crystals. The absorbance of the samples at 490 nm was recorded with a multimode microplate reader (Infinite M200 PRO, Tecan).

Molecular dynamic simulations

Molecular dynamic simulations by GROMACS 5.1[9-15] with amber99sb force field were performed to sample the interaction mode between hemin and G-quadruplex. The force field parameters of hemin were generated by antechamber[16] program of AmberTool6 software[17] and converted to GROMACS topology format by acpype[18] program. RESP atom charges of hemin were calculated by Gaussian 09 program[19] at the level of B3LYP[20, 21]/6-311++G(2d,2p)[22-26]. The parameters of ferric ion were taken from our previous work.[27] SPC/E water model[28] was used as the solvent and sodium cation was used as counterions for neutralization only (We have also used potassium cation to neutralize the model systems, and similar results were obtained). The bonded parameters of hydrogen peroxide were retrieved from work of Margulis[29] and force constant of torsion (HOOH) was increased by three times.[30] The nonbonded parameters were the same as those in the work of Lv et al.[31] Distance constraints (2.0 Å) between ferric cation and four near nitrogen atoms were applied for the

simulations containing hydrogen peroxide in order to place ferric cation in the center of hemin ring.

The initial structures of parallel folded G-quadruples were generated by 3D-NuS tool.[32] In each bound model system, the G-quadruplex molecule was placed on hemin with either its 5'- or 3'-end interacting with hemin. These model systems were then subject to plain simulations, and the ones that were stable during the whole simulations were chosen for further analysis. The models with a hydrogen peroxide molecule at the distal position were prepared from the corresponding water-bound models by replacing the bridging water molecule between hemin and G-quadruplex with a hydrogen peroxide molecule. Three sodium or potassium cations were inserted into the center of each G-quadruple to bridge the four G residues. We have done the simulations with and without hemin to identify the most stable conformation of each G-quadruplex model. We have also done the simulations in the presence of H_2O_2 and found that the dynamics of the model systems was similar to that in the absence of H_2O_2.

Periodic boundary condition (PBC) was imposed on all three dimensions during the simulations through cube box (edge length range in 54-61 Å). Prior to production runs, the model systems were first relaxed by steepest descent algorithm followed by equilibration under NVT and then NPT ensemble with each for 100 ps, with the temperature at 300 K by velocity rescaling thermostat[33] with coupling time of 0.1 ps and pressure at 1 bar by Parrinello-Rahman[34, 35] algorithm with coupling time of 2 ps. All model systems were sampled for 100 ns.

The long-range electrostatics were calculated by smooth particle mesh Ewald (PME)[36, 37] method and a cutoff of 1.0 nm was used for both electrostatics and van der Waals. During simulations, the LINCS[38] algorithm was employed to constrain all bonds involving hydrogen atom to qualify a step size of 2 fs in the integration with leap-frog integrator. The trajectory was saved every 500 steps (i.e. 1.0 ps) for analysis.

The orientation of the coordinated water molecule and hydrogen peroxide at the distal site was used in rotational correlation function calculations.

After simulations, several post-analysis procedures were performed to investigate the properties of the model systems. Atomic positional root mean square deviation (RMSD) was calculated to evaluate the stability of the whole system, and all non-hydrogen atoms were considered. Inter-plane distance between hemin and the G-quadruple plane was used to measure the space between them, which was combined with co-plane index (each plane defined by three atoms) to show the stability of interaction between hemin and G-quadruplex. Rotational correlation function (use vector perpendicular to water plane) and hydrogen bond analysis (GROMACS convention, i.e. $R \leq 3.5$ Å, $\alpha \leq 30^{o}$) involved bridging water to depict their motion. We also calculated solvent accessible surface area (SASA) of G-quadruplex to assess their contact with the bulk. In the end, we did energy decomposition analysis as implemented in GROMACS MD engine to find out the interaction component contributions (include electrostatic and van der Waals) to the binding. During the analysis, the calculations of rotational correlation function, co-plane index, inter-plane distance and hydrogen bonds were conducted by an in-house program CAC-ANA.

The prototype DNA molecules in experimental studies, labeled as G4-1 and G4-2, respectively, were used in the MD simulations. Four models were prepared with the two DNA molecules interacting a hemin molecule with (hemin-G4-1 and hemin-G4-2) or without (hemin/G4-1 and hemin/G4-2) an alkyl linker.

The definition and meaning of relevant parameters in molecular dynamic simulations:

Atomic positional root mean square deviation (RMSD) is used to show the fluctuation of the system during a simulation.

Coplanarity describes how much G residues stay in a plane.

Coplane index (CPI) is a descriptor describing the coplanarity with 1 meaning the coplanarity and 0 nonplanarity.

The standard deviation of CPI (STDCPI) is the standard deviation of the coplane indices.

Energy decomposition analyzes the decomposition of interaction energies between particles according to the energy terms in the force field.

The inter-plane distance is the distance between two planes.

Solvent accessible surface area (SASA) analysis is to evaluate the surface area of a model system.

The longer rotational relaxation time describes the character of the rotational motion of a specific vector.

Hydrogen bond distance is the distance between the donor atom (which contributes proton) and the H-bond acceptor atom (O, N).

Fe-O distance between hemin and water is the distance of the coordination bond between ferric ion and the coordinating oxygen atom of water molecule.

Umbrella Sampling

Umbrella sampling technique was used to calculate the binding affinity of hemin with G-quadruplex in the two noncovalently bound models. The intermolecular distance between hemin and G-quadruplex, defined by the distance between their centers of mass, was used as the reaction coordinate ξ.

For each umbrella sampling case, the steered molecular dynamics was performed by using harmonic potential with force constant of 10000 $kJ \cdot mol^{-1} \cdot nm^{-2}$ and rate of 0.001 nm/ns to generate starting conformations from binding state to dissociated state. The extracted conformations (distance interval of 0.05 nm) were saved and equilibrated in an NPT ensemble for 1 ns, and the reaction coordination was

constrained by a harmonic potential with a force constant of 5000 $kJ \cdot mol^{-1} \cdot nm^{-2}$. This was followed by a 10-ns sampling. Other simulation parameters were the same as in the plain MD simulations mentioned above.

The Gibbs free energy profiles were retrieved by weighted histogram analysis method (WHAM)[39] implemented in GROMACS (g_wham[40]), and the profile curves were smoothed by B-spline interpolation.

Statistical analysis

All data were expressed as mean ± SD of at least three independent experiments. The differences between two groups were analyzed by two-tailed Student's *t*-test.

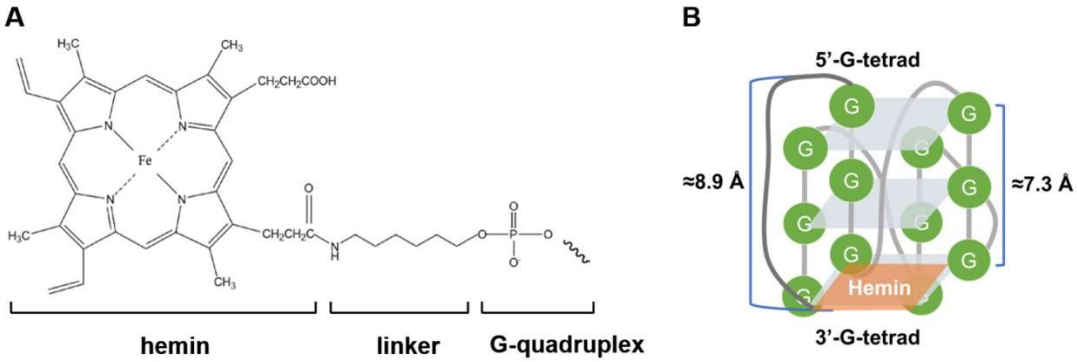

Figure S1. Chemical structure of 5' hemin-modified G-quadruplex (A) and cartoon illustration of hemin-G-quadruplex (B).

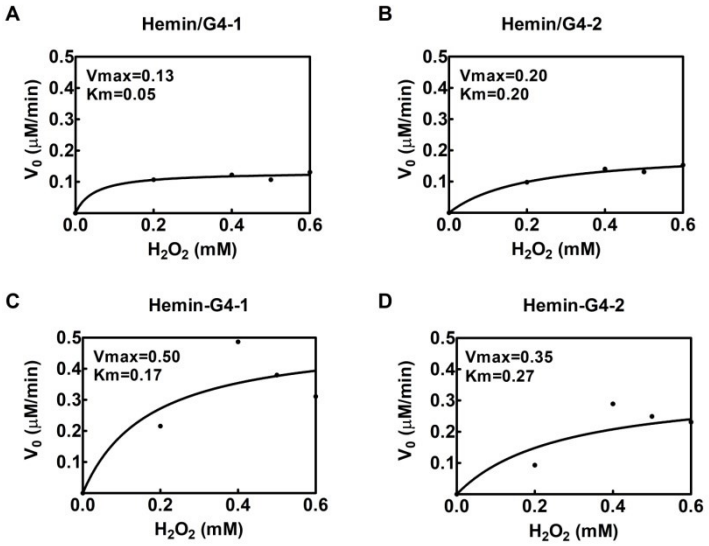

Figure S2. Plots of the initial velocity (V_0) as a function of hydrogen peroxide concentration for the DNAzymes Hemin/G4-1 (A), Hemin/G4-2 (B), Hemin-G4-1 (C) and Hemin-G4-2 (D). The Michaelis constant (K_m) is the hydrogen peroxide concentration at which the reaction velocity is half of V_{max}.

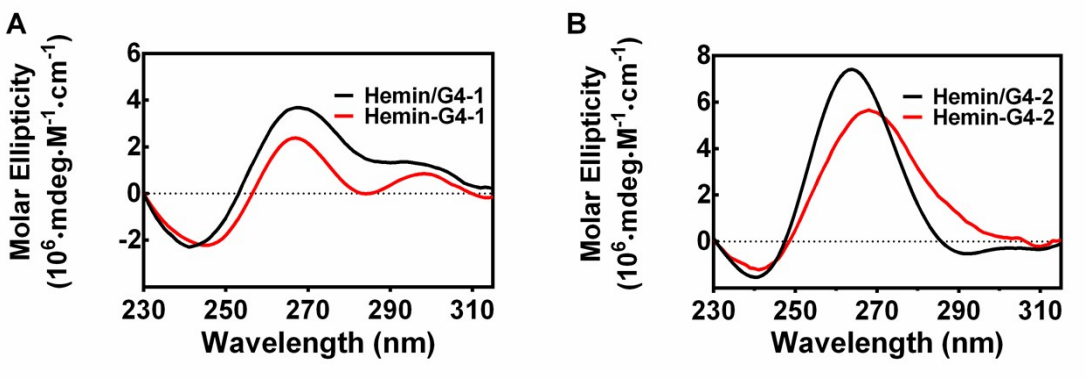

Figure S3. Circular dichroism (CD) spectra of four G-quadruplex/hemin complexes.

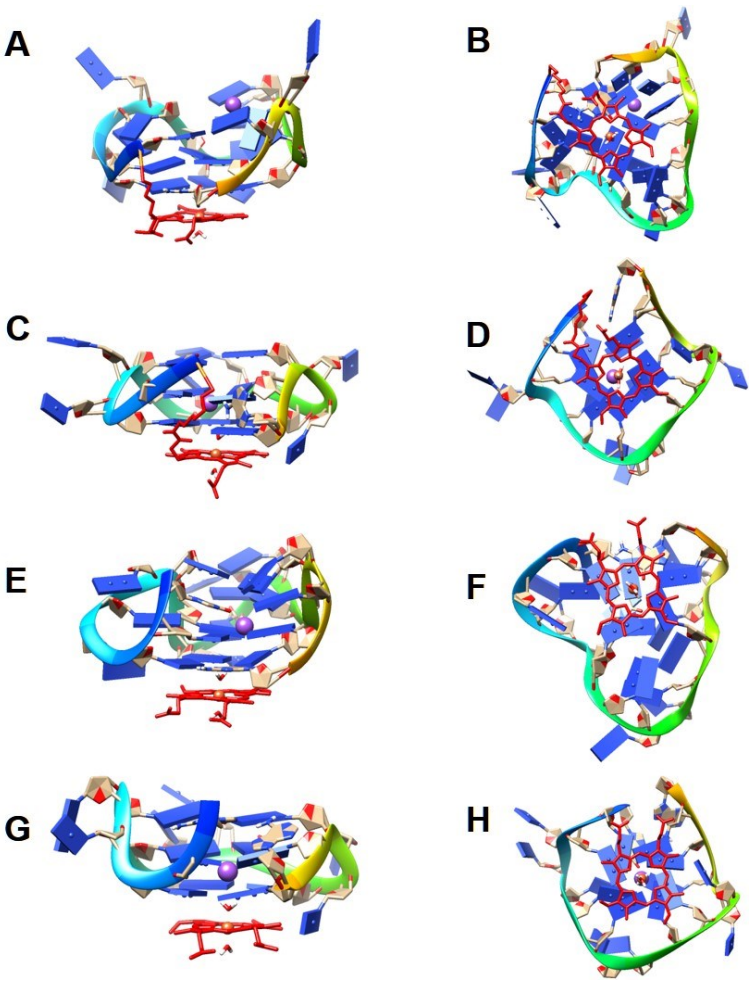

Figure S4. Side (A, C, E, G) and top (B, D, F, H) views of the last snapshot of Hemin-G4-1 (A and B), Hemin-G4-2 (C and D), Hemin/G4-1 (E and F) and Hemin/G4-2 (G and H) complexes after 100-ns sampling. The molecular structures were rendered by Chimera 1.14.

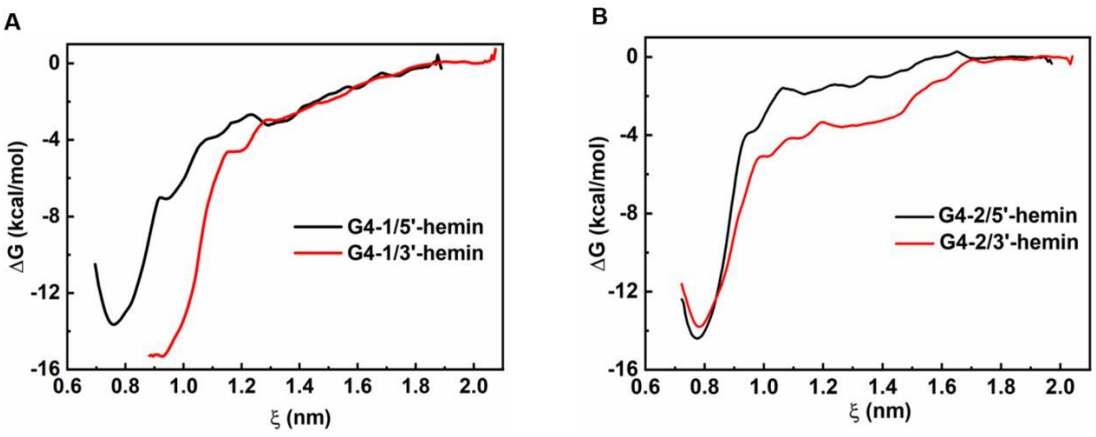

Figure S5. Gibbs free energy profiles of Hemin/G4-1 (A) and Hemin/G4-2 (B) from umbrella sampling of hemin approaching 5'-end or 3'-end of the G-quadruplex.

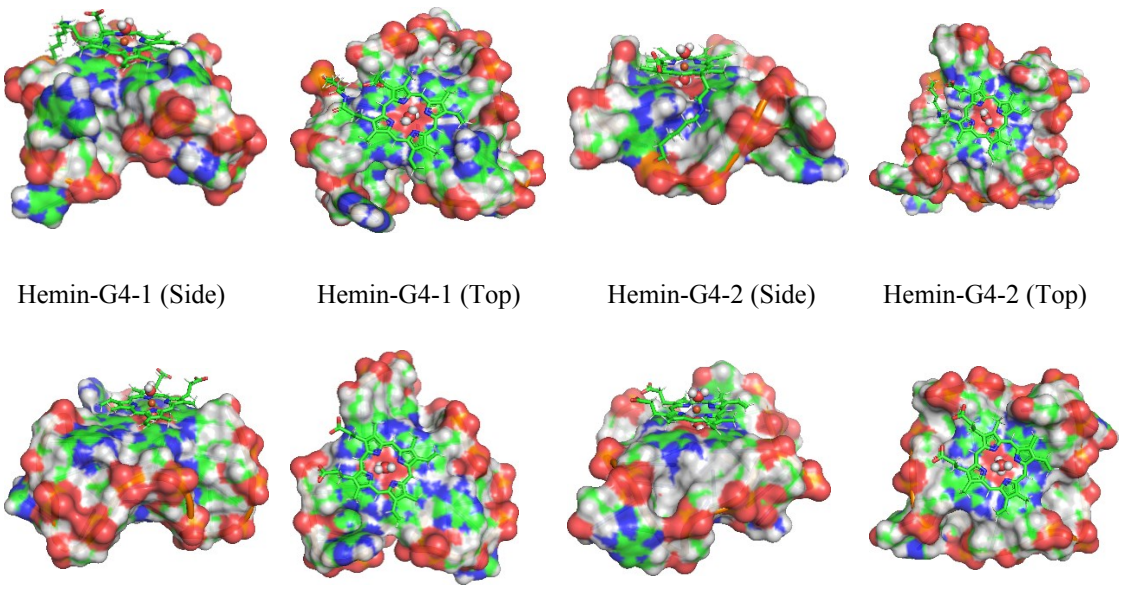

Figure S6. Surface views of model systems with bridging water inside.

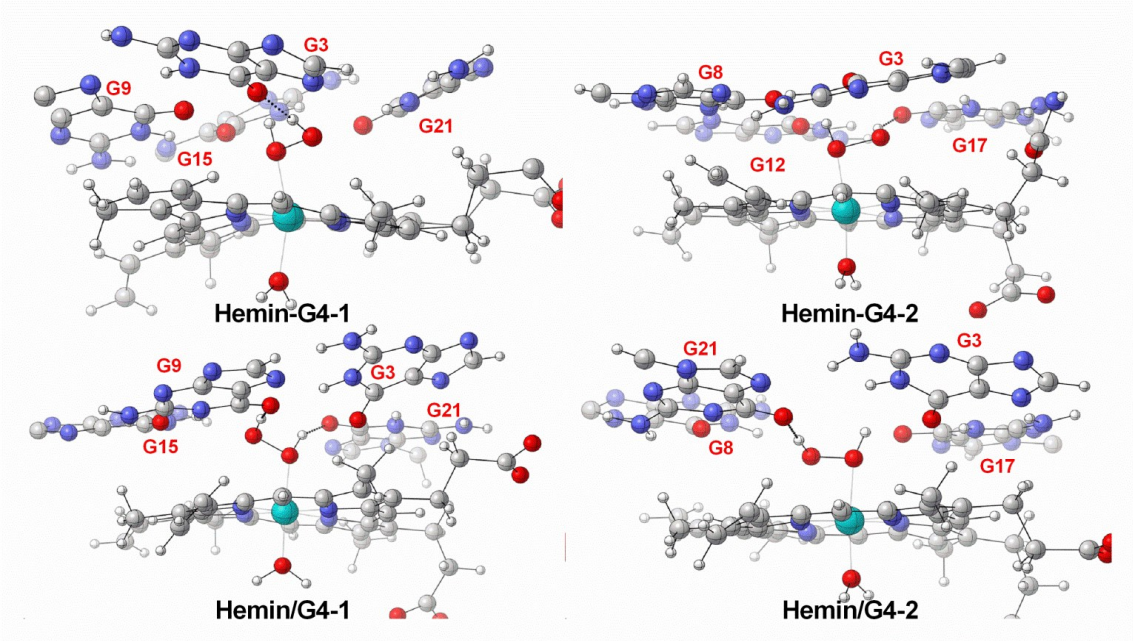

Figure S7. Representative snapshots to demonstrate the interaction modes of DNAzymes intercalated with a hydrogen peroxide molecule. Ferric ions are labeled in sapphire.

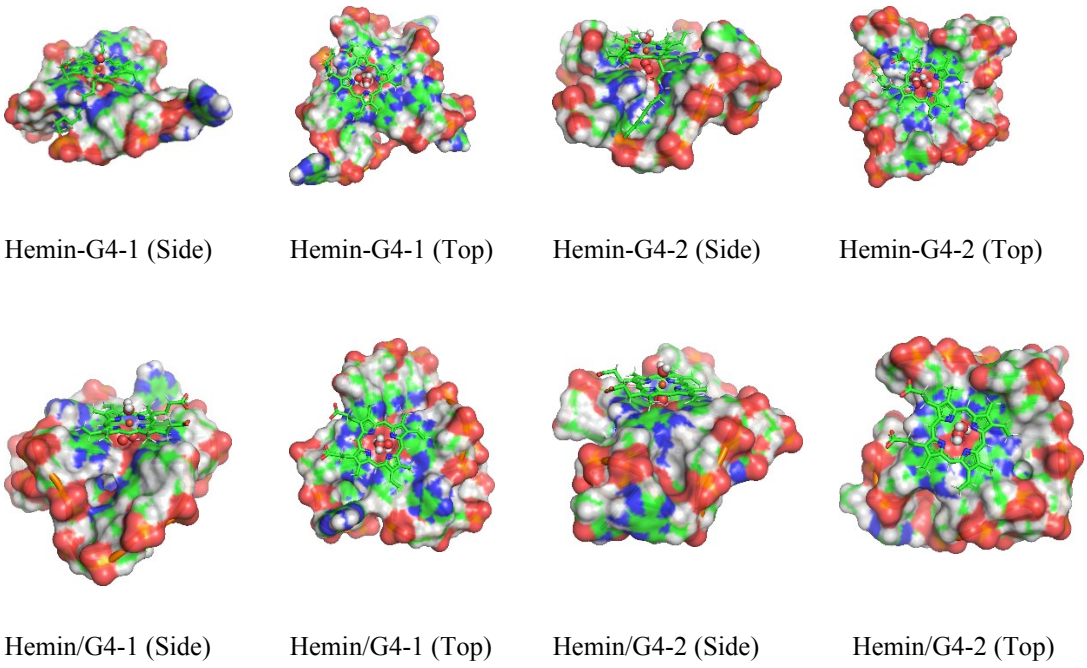

Figure S8. Surface views of model systems with bridging hydrogen peroxide inside.

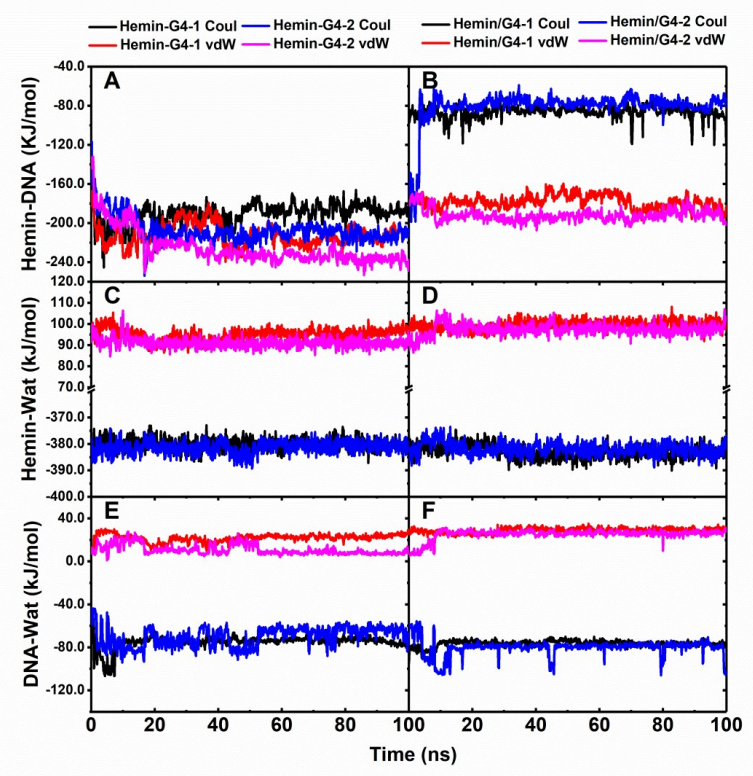

Figure S9. Energy decomposition in the 100-ns simulation. Wat indicates the water molecule between G-quadruplex and hemin. Coul: Coulomb force; vdW: van der Waals force.

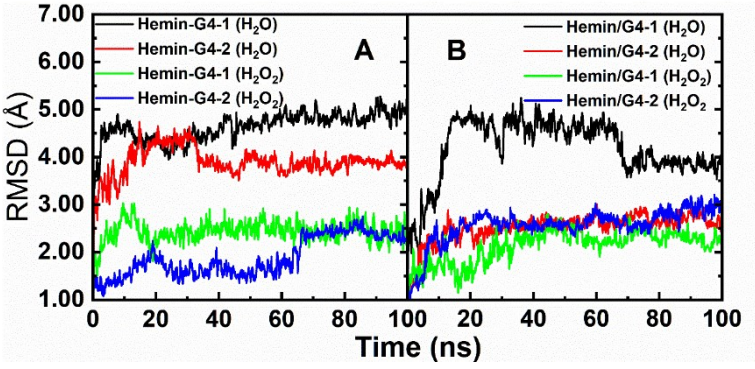

Figure S10. RMSD of Hemin-G4 (A) and Hemin/G4 (B). Only non-hydrogen atoms were considered in the calculations.

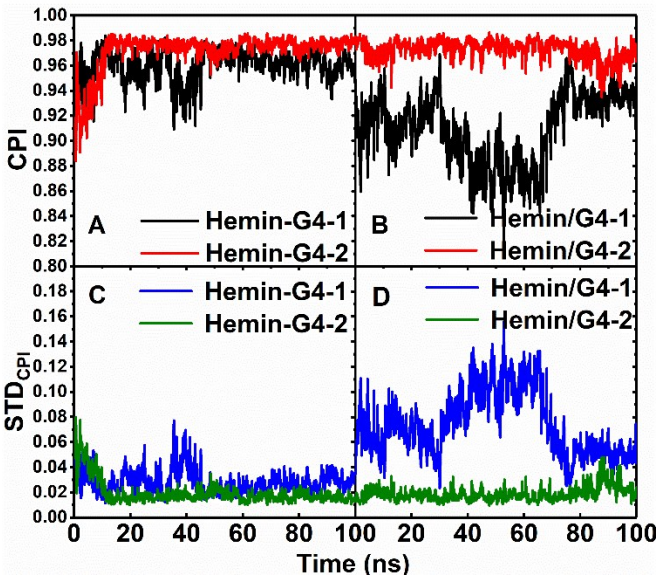

Figure S11. Co-plane index (top) and its standard deviation (bottom) of the G-quartet plane in DNAzymes with bridging water. The data were averaged for every 100 ps.

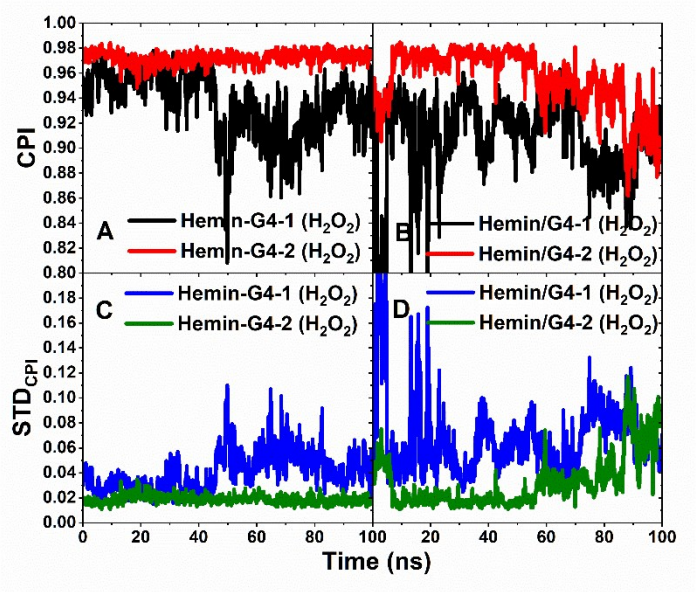

Figure S12. Co-plane index (top) and its standard deviation (bottom) of the G-quartet plane in DNAzymes with bridging hydrogen peroxide. The data were averaged for every 100 ps.

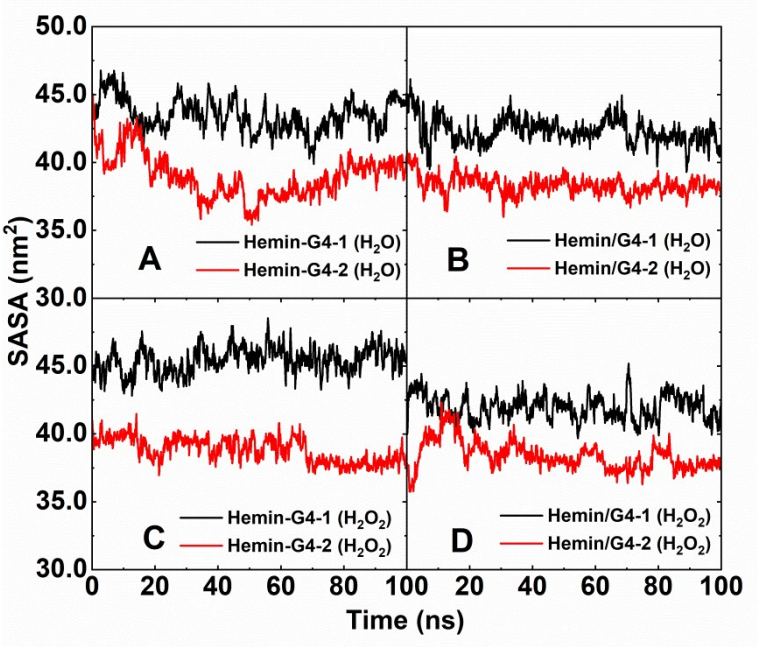

Figure S13. Solvent access surface area (SASA) during the 100-ns simulation for Hemin-G4 and Hemin/G4 complexes bridged by water or hydrogen peroxide (Averaged for every 100 ps, including hydrogen atoms and without iron).

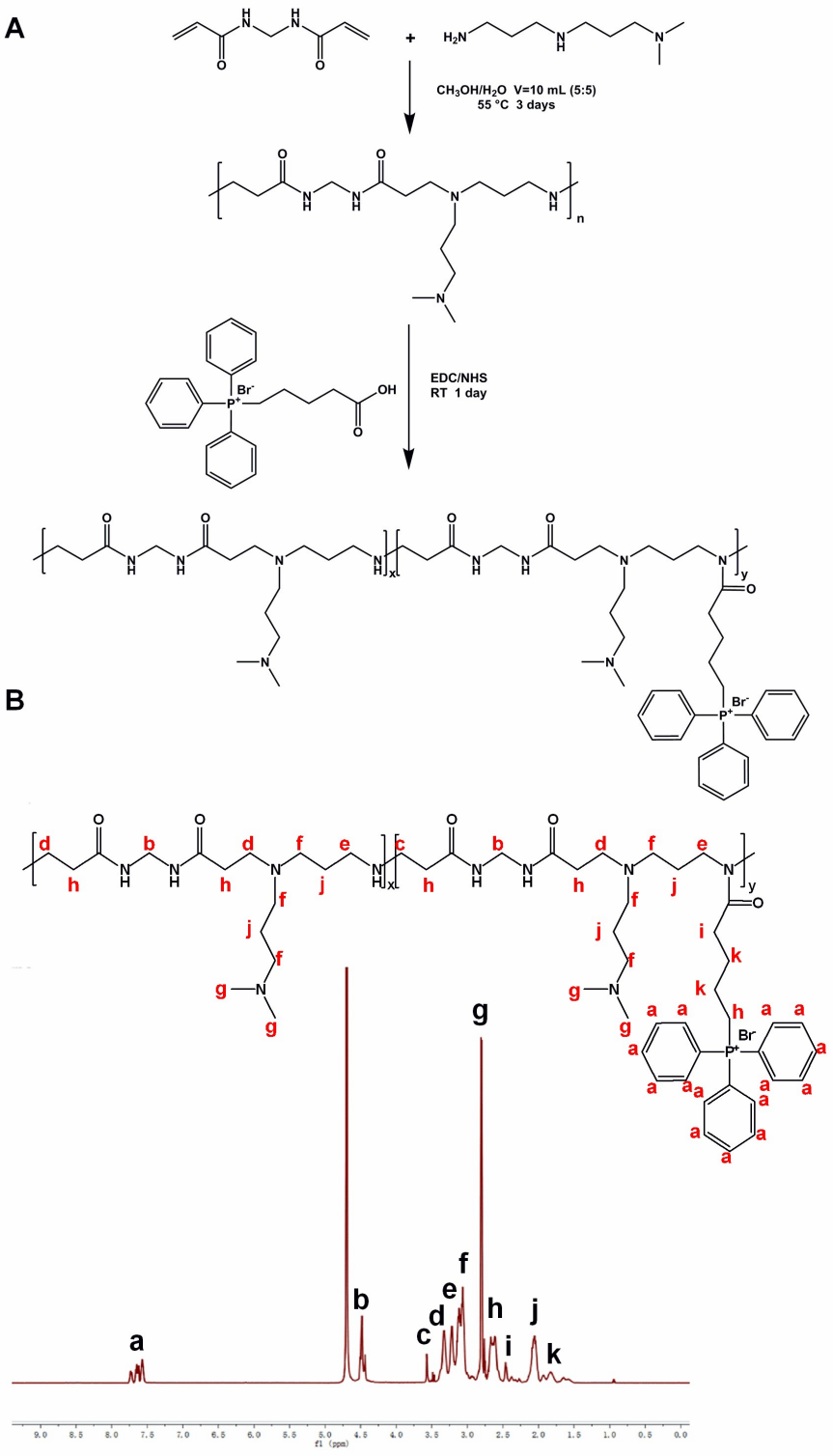

Figure S14. Synthesis of TPAA polymer (A) and its ^{1}H NMR spectrum recorded by a Bruker Super Conducting Fourier NMR Spectrometer (AVANCE IIITM 500 MHz) (B).

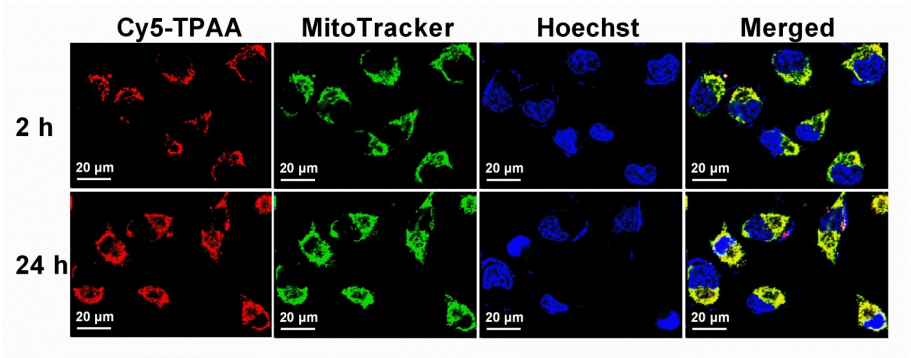

Figure S15. Confocal images of Cy5-TPAA and MitoTracker Green in HeLa cells. Pearson's correlation coefficients for colocalization were 0.836 (2 h) and 0.95 (24 h). Cell nuclei were stained by Hoechst 33342 (blue). The scale bars are 20 μm.

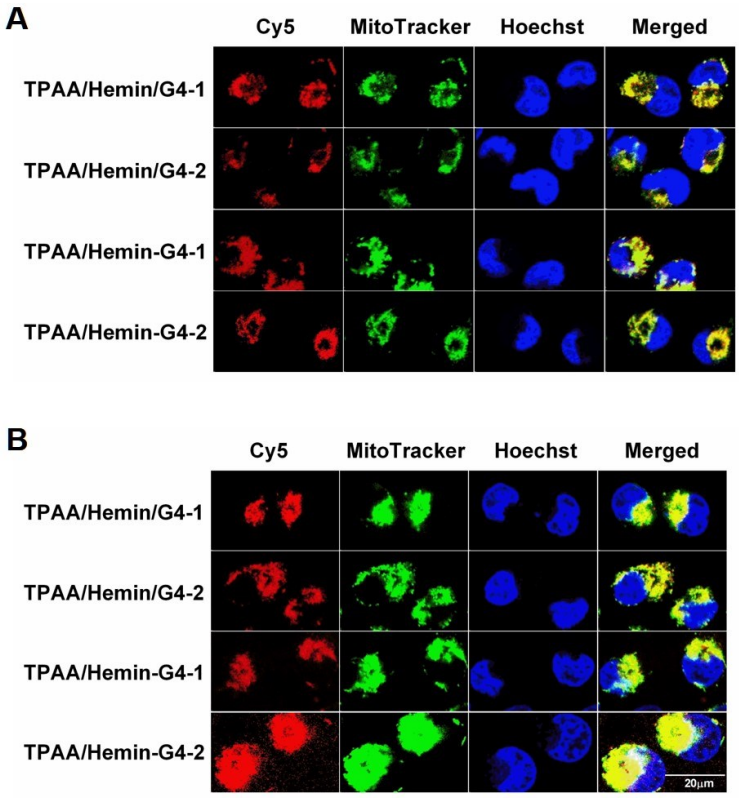

Figure S16. Confocal images of Cy5-TPAA/DNAzymes (red) and MitoTracker Green (green) in HeLa cells at 2 h (A) and 6 h (B). Cell nuclei were stained by Hoechst 33342 (blue). Scale bar = 20 μm.

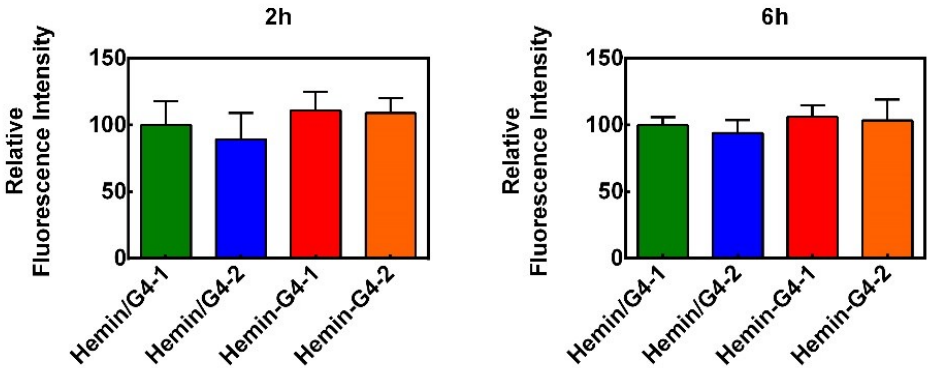

Figure S17. Relative fluorescence intensity of Cy5-labeled TPAA/DNAzymes in HeLa cells. $n = 3$.

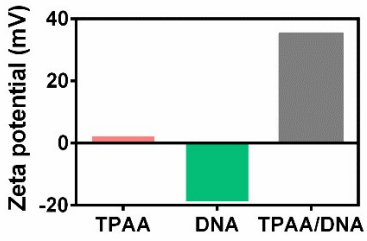

Figure S18. Zeta potentials of TPAA, DNA and TPAA/DNA in acetate buffer, pH 5.0. G4-1 was used as a DNA model.

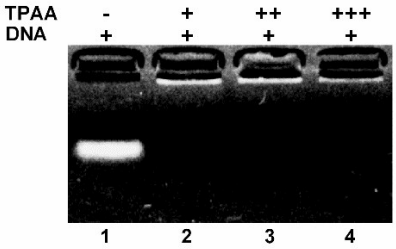

Figure S19. The capability of TPAA to condense DNA was analyzed. Lane 1, naked DNA (G4-1). Lanes 2 - 4, DNA (G4-1) was condensed by TPAA with the N/P ratios of 5/1, 10/1, 20/1, respectively.

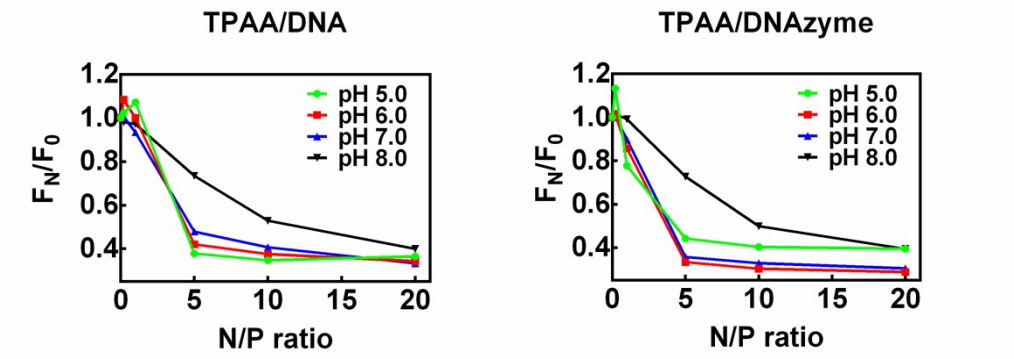

Figure S20. The nucleic acid dye displacement assays. DNA or DNAzyme was combined with nucleic acid dye at pH (5.0, 6.0, 7.0, 8.0) and TPAA was then added with the N/P ratios of 0.2/1, 1/1, 5/1, 10/1, 20/1.

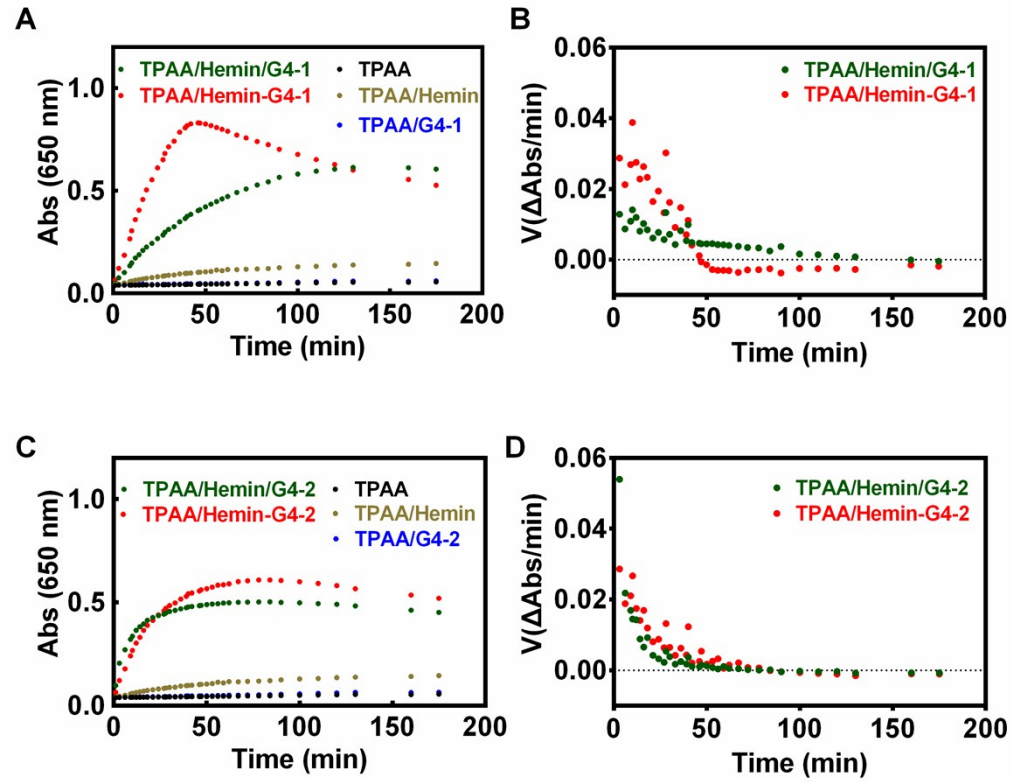

Figure S21. TMB absorbance intensity after incubating with the DNAzymes encapsulated by TPAA polymers. The absorbance was monitored in 175 min for G4-1-based DNAzymes (A) and G4-2-based DNAzymes (C). The time course of absorbance change was analyzed for G4-1-based DNAzymes (B) and G4-2-based DNAzymes (D).

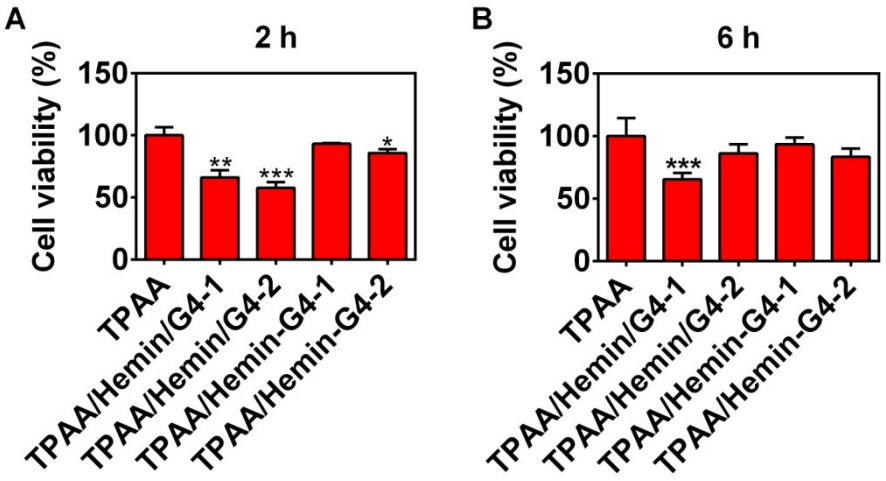

Figure S22. The cytotoxicity of DNAzymes in HeLa cells was analyzed with MTT assays at 2 h (A) and 6 h (B). * $P < 0.05$, ** $P < 0.01$, *** $P < 0.001$, $n = 6$.

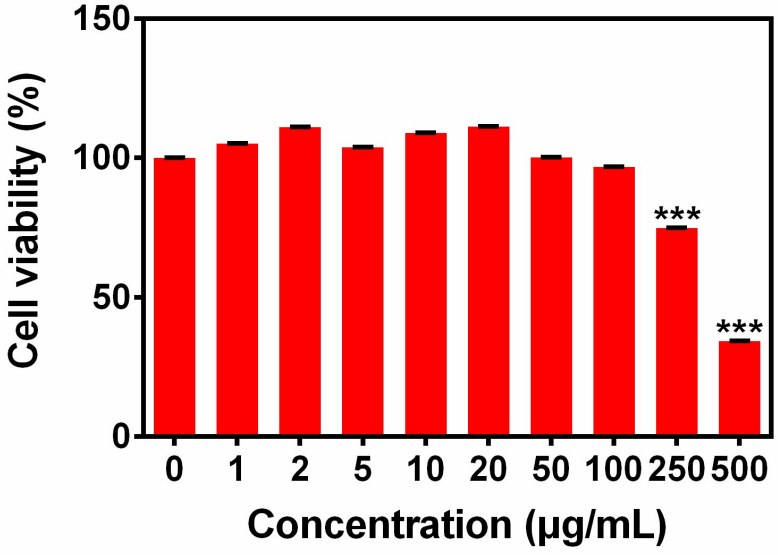

Figure S23. The cytotoxicity of TPAA in HeLa cells was examined with MTT assays at 24 h. *** $P < 0.001$, $n = 6$.

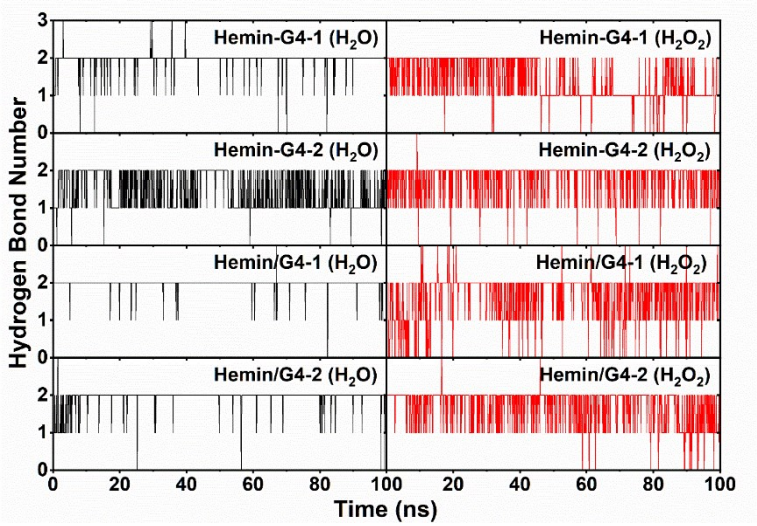

Figure S24. Hydrogen bond number between DNA and hydrogen peroxide (or water) bound on hemin during the 100-ns simulation for hemin-G4 and hemin/G4 complexes (every 100 ps).

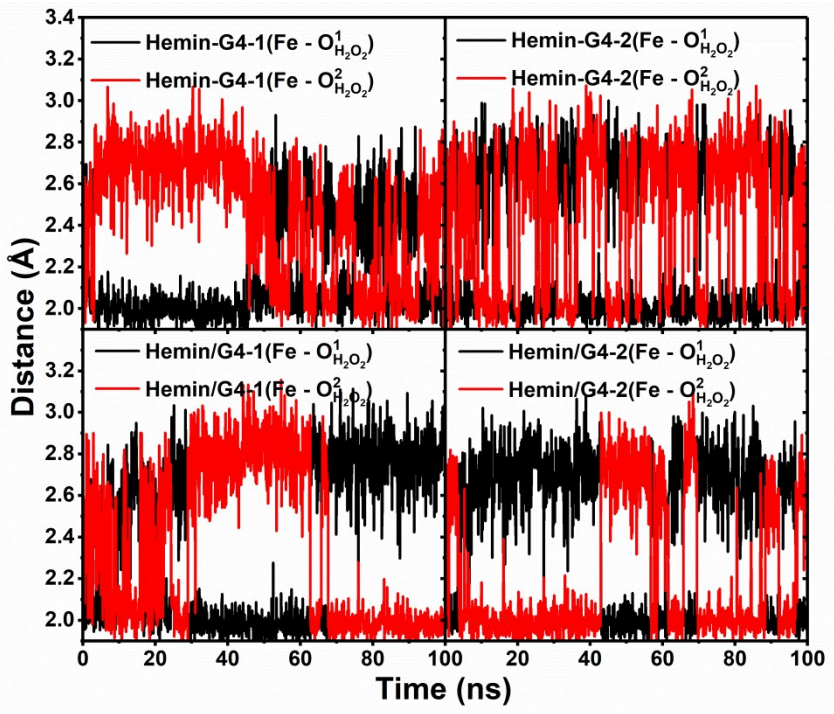

Figure S25. Fe-O distance between hemin and hydrogen peroxide in DNAzymes as a function of time during the 100-ns simulation. O1 H_2O_2 and O2 H_2O_2 represent two O atoms of hydrogen peroxide.

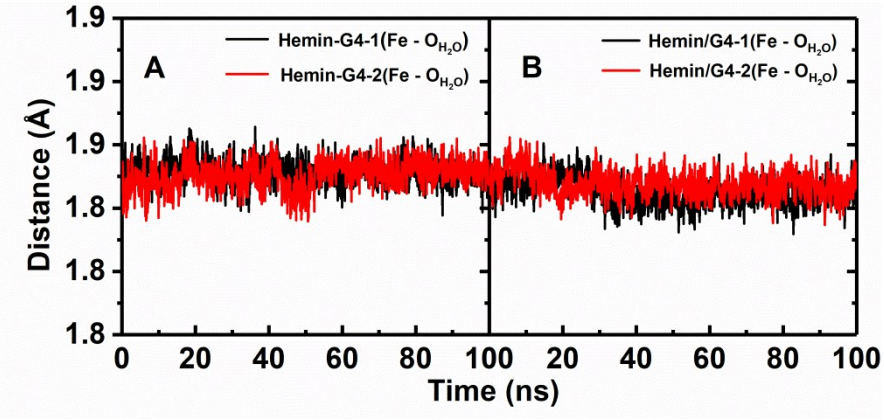

Figure S26. Fe-O distance between hemin and water in DNAzymes as a function of time during the 100-ns simulation. OH_2O represents the O atom of water.

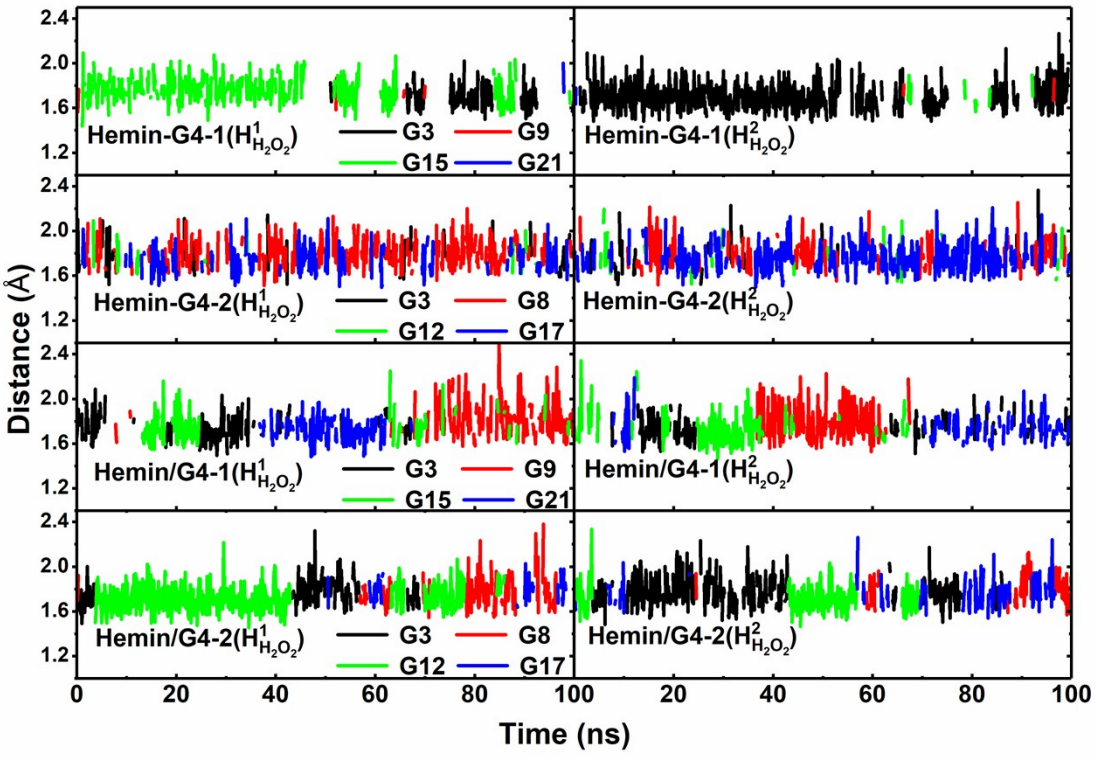

Figure S27. Hydrogen bond distance (hydrogen – acceptor) between G-quadruplex and hydrogen peroxide in DNAzymes as a function of time during the 100-ns simulation. H1 H_2O_2 and H2 H_2O_2 represent two H atoms of hydrogen peroxide.

Extended discussion

In physiological conditions, ROS generation in mitochondria is delicately controlled to avoid too much ROS being produced. When ROS-reactive agents are sent to mitochondria, excess ROS will be generated which can damage mitochondria. The damaged mitochondria will leak more ROS from the respiratory chain. Excess ROS and damaged mitochondria form a vicious circle. As a result, ROS-reactive agents can elicit the "domino effect" of ROS burst in mitochondria.[41] Since DNAzymes can decompose hydrogen peroxide, it can also be potentially used for inducing ROS burst and damaging mitochondria in cancer cells. The damaged mitochondria will ultimately lead to apoptosis of cancer cells. To achieve this goal, a prerequisite is to find a DNAzyme that is stable and active in mitochondria. This study has demonstrated that the activity of DNAzyme in mitochondria cannot be simply extrapolated from the DNAzyme activity *in vitro*. The proximity and interaction mode of hemin and G-quadruplex should be considered.

The decomposition of H_2O_2 by the DNAzyme can generate superoxide (O_2^-).[42] (1) DNAzyme + H_2O_2 →compound I + H_2O; (2) compound I + H_2O_2 → compound II + O_2^-. For assaying the DNAzyme activity in mitochondria, we examined the levels of superoxide, instead of substrate oxidation. There are many reducing substances that can be potentially oxidized by the DNAzyme inside the cell, and it may not be easy to assay all of them. In addition, a previous study suggested that the peroxidase-like activity of DNAzyme primarily depends on H_2O_2 availability and is independent of the peroxidase substrate.[43] Therefore, we examined the levels of superoxide in cells to indicate the catalytic activity of DNAzymes by using the mitochondria-targeted probe MitoSOX. MitoSOX can be rapidly oxidized by superoxide, but not by other ROS or reactive nitrogen species (RNS). According to Figure 4, the baseline levels of superoxide in mitochondria were relatively low. DNAzyme-induced production of superoxide could be visualized by the superoxide probe MitoSOX.

After we found the difference in activity of the DNAzyme between *in vitro* and in mitochondria, we resorted to molecular dynamic simulations for illustrating how the

interaction modes of DNAzymes correlate with the DNAzyme activity. In theoretical calculations, we took the full length of G-quadruplex sequence into account. We mainly elaborated on the interaction of G-tetrad with hemin, since this is the reaction center of the DNAzyme that is commonly presented in both G4-1 and G4-2-derived DNAzymes. How other nucleotides in G-quadruplex modulate the DNAzyme activity in mitochondria warrants further investigation. It may entail activity screening of a number of structurally different DNAzymes in mitochondria.

For DNAzyme modeling, we modeled the binding of hemin to the 3'-end of G-quadruplex in both the noncovalently and covalently bound complexes for the following reasons. First, accumulating evidence indicates that free hemin preferentially binds to the 3'-end of G-quadruplex.[4, 44-46] Moreover, it has been suggested that hemin at the 3'-end of G-quadruplex is more catalytically competent than hemin at the 5'-end.[47] Second, we analyzed the evolution of the potentials of mean force along the pathways of the two binding modes. As shown in Figure S5, the reaction coordinate ξ was defined as the distance between the iron site and the center of G4-1 or G4-2. The evolution of the potentials of mean force showed that on the way to approaching each other, there was more free energy gain in the 3'-terminus binding mode than the 5'-terminus binding mode. These results suggested that the motion of G-quadruplex with its 3'-terminus heading to hemin is kinetically favored. Third, the length of the linker was estimated to be ca. 8.9 Å, which is longer than the length of the three layers of the G-tetrad (ca. 7.3 Å). Since the linker is composed of unsubstituted C atoms, it tends to adopt an extended conformation (Figure S1). These results suggested that the linker predisposes hemin to the 3'-end of G-quadruplex. Our data were in agreement with the previous study that the linker with proper length (~6-atom-long) is favorable to the activity of the DNAzyme.[48] Taken together, both free hemin and covalently bound hemin preferentially bind to the 3'-end of G-quadruplex, because hemin/3' G-quadruplex is kinetically stable and catalytically competent.

References

1. Z. Y. Wang, J. Zhao, J. C. Bao and Z. H. Dai, *ACS Appl. Mater. Interfaces*, 2016, **8**, 827-833.
2. J. Y. Zhang, K. W. Zheng, S. Xiao, Y. H. Hao and Z. Tan, *J. Am. Chem. Soc.*, 2014, **136**, 1381-1390.
3. B. L. Li, Y. Du, T. Li and S. J. Dong, *Anal. Chim. Acta*, 2009, **651**, 234-240.
4. Y. H. Guo, J. L. Chen, M. P. Cheng, D. Monchaud, J. Zhou and H. X. Ju, *Angew. Chem. Int. Ed.*, 2017, **56**, 16636-16640.
5. J. Chen, X. Qiu, J. Ouyang, J. Kong, W. Zhong and M. M. Xing, *Biomacromolecules*, 2011, **12**, 3601-3611.
6. J. Chen, C. Wu and D. Oupicky, *Biomacromolecules*, 2009, **10**, 2921-2927.
7. A. J. Geall and I. S. Blagbrough, *J. Pharm. Biomed. Anal.*, 2000, **22**, 849-859.
8. H. Huang, J. Chen, H. R. Lu, M. X. Zhou, Z. F. Chai and Y. Hu, *Biometals*, 2017, **30**, 623-628.
9. M. J. Abraham, T. Murtola, R. Schulz, S. Páll, J. C. Smith, B. Hess and E. Lindahl, *SoftwareX*, 2015, **1-2**, 19-25.
10. S. Páll, M. J. Abraham, C. Kutzner, B. Hess and E. Lindahl, International Conference on Exascale Applications and Software, Stockholm, Sweden, 2014.
11. S. Pronk, S. Páll, R. Schulz, P. Larsson, P. Bjelkmar, R. Apostolov, M. R. Shirts, J. C. Smith, P. M. Kasson and D. van der Spoel, *Bioinformatics*, 2013, **29**, 845-854.
12. B. Hess, C. Kutzner, D. Van Der Spoel and E. Lindahl, *J. Chem. Theory Comput.*, 2008, **4**, 435-447.
13. D. Van Der Spoel, E. Lindahl, B. Hess, G. Groenhof, A. E. Mark and H. J. Berendsen, *J. Comput. Chem.*, 2005, **26**, 1701-1718.
14. H. J. Berendsen, D. van der Spoel and R. van Drunen, *Comput. Phys. Commun.*, 1995, **91**, 43-56.
15. E. Lindahl, B. Hess and D. van der Spoel, *J. Mol. Model.*, 2001, **7**, 306-317.
16. J. Wang, R. M. Wolf, J. W. Caldwell, P. A. Kollman and D. A. Case, *J. Comput. Chem.*, 2004, **25**, 1157-1174.
17. D. A. Case, R. M. Betz, W. Botello-Smith, D. S. Cerutti, T. E. Cheatham, III, T. A. Darden, R. E. Duke, T. J. Giese, H. Gohlke, A. W. Goetz, N. Homeyer, S. Izadi, P. Janowski and J. Kaus, *Amber* (version 2016), University of California: San Francisco, CA., 2016.
18. A. W. Sousa da Silva and W. F. Vranken, *BMC Res. Notes*, 2012, 5, 367.
19. M. J. Frisch, G. W. Trucks, H. B. Schlegel, G. E. Scuseria, M. A. Robb, J. R. Cheeseman, G. Scalmani, V. Barone, B. Mennucci, G. A. Petersson, H. Nakatsuji, M. Caricato, X. Li, H. P. Hratchian, A. F. Izmaylov, J. Bloino, G. Zheng, J. L. Sonnenberg, M. E. Hada, M., K. Toyota, R. Fukuda, J. Hasegawa, M. Ishida, T. Nakajima, Y. Honda, O. Kitao, H. Nakai, T. Vreven, J. A. Montgomery, Jr., J. E. Peralta, F. Ogliaro, M. Bearpark, J. J. Heyd, E. Brothers, K. N. Kudin, V. N. Staroverov, R. Kobayashi, J. Normand, K. Raghavachari, A. Rendell, J. C. Burant, S. S. Iyengar, J. Tomasi, M. Cossi, N. Rega, J. M. Millam, M. Klene, J. E. Knox, J. B. Cross, V. Bakken, C. Adamo, J. Jaramillo, R. Gomperts, R. E. Stratmann, O. Yazyev, A. J. Austin, R. Cammi, C. Pomelli, J. W. Ochterski, R. L. Martin, K. Morokuma, V. G. Zakrzewski, G. A. Voth, P. Salvador, J. J. Dannenberg, S.

Dapprich, A. D. Daniels, O. Farkas, J. B. Foresman, J. V. Ortiz, J. Cioslowski and D. J. Fox, *Gaussian 09* (Revision C.01)*,* Gaussian, Inc.: Wallingford, CT, 2009.
20. R. G. Parr and W. Yang, *Density Functional Theory of Atoms and Molecules*, Oxford University Press, New York, 1989.
21. P. Bultinck, H. D. Winter, W. Langenaeker and J. P. Tollenare, *Computational Medicinal Chemistry for Drug Discovery*, CRC Press, Boca Raton, 2003.
22. W. J. Hehre, R. Ditchfield and J. A. Pople, *J. Chem. Phys.*, 1972, **56**, 2257-2261.
23. P. C. Hariharan and J. A. Pople, *Theor. Chem. Acc.*, 1973, **28**, 213-222.
24. G. W. Spitznagel, T. Clark, P. V. Schleyer and W. J. Hehre, *J. Comput. Chem.*, 1987, **8**, 1109-1116.
25. T. Clark, J. Chandrasekhar, G. W. Spitznagel and P. V. Schleyer, *J. Comput. Chem.*, 1983, **4**, 294-301.
26. P. C. Hariharan and J. A. Pople, *Mol. Phys.*, 1974, **27**, 209-214.
27. M. Xia, Z. Chai and D. Wang, *J. Phys. Chem. B*, 2017, **121**, 5718-5729.
28. H. Berendsen, J. Grigera and T. Straatsma, *J. Phys. Chem.*, 1987, **91**, 6269-6271.
29. Y.-H. Chung, J. Xia and C. J. Margulis, *J. Phys. Chem. B*, 2007, **111**, 13336-13344.
30. J. Koput, S. Carter and N. C. Handy, *J. Phys. Chem. A*, 1998, **102**, 6325-6330.
31. Y. Lv, X. Wang, X. Yu, S. Zheng, S. Wang, Y. Zhang and H. Du, *Phys. Chem. Chem. Phys.*, 2017, **19**, 7054-7061.
32. L. P. P. Patro, A. Kumar, N. Kolimi and T. Rathinavelan, *J. Mol. Biol.*, 2017, **429**, 2438-2448.
33. G. Bussi, D. Donadio and M. Parrinello, *J. Chem. Phys.*, 2007, **126**, 014101.
34. M. Parrinello and A. Rahman, *J. Appl. Phys.*, 1981, **52**, 7182-7190.
35. S. Nosé and M. Klein, *Mol. Phys.*, 1983, **50**, 1055-1076.
36. U. Essmann, L. Perera, M. L. Berkowitz, T. Darden, H. Lee and L. G. Pedersen, *J. Chem. Phys.*, 1995, **103**, 8577-8593.
37. T. Darden, D. York and L. Pedersen, *J. Chem. Phys.*, 1993, **98**, 10089-10092.
38. B. Hess, H. Bekker, H. J. Berendsen and J. G. Fraaije, *J. Comput. Chem.*, 1997, **18**, 1463-1472.
39. S. Kumar, D. Bouzida, R. H. Swendsen, P. A. Kollman and J. M. Rosenberg, *J. Comput. Chem.*, 1992, **13**, 1011-1021.
40. J. S. Hub, B. L. de Groot and D. van der Spoel, *J. Chem. Theory Comput.*, 2010, **6**, 3713-3720.
41. Y. Liu, H. P. Li, J. Xie, M. X. Zhou, H. Huang, H. R. Lu, Z. F. Chai, J. Chen and Y. Hu, *Biomater. Sci.*, 2017, **5**, 1022-1031.
42. X. J. Yang, C. L. Fang, H. C. Mei, T. J. Chang, Z. H. Cao and D. H. Shangguan, *Chem. Eur. J.*, 2011, **17**, 14475-14484.
43. T. Li, S. J. Dong and E. K. Wang, *Chem.-Asian J.*, 2009, **4**, 918-922.
44. W. Li, Y. Li, Z. Liu, B. Lin, H. Yi, F. Xu, Z. Nie and S. Yao, *Nucleic Acids Res.*, 2016, **44**, 7373-7384.
45. Y. Yamamoto, H. Araki, R. Shinomiya, K. Hayasaka, Y. Nakayama, K. Ochi, T. Shibata, A. Momotake, T. Ohyama, M. Hagihara and H. Hemmi, *Biochemistry*, 2018, **57**, 5938-5948.

46. Y. W. Cao, P. Ding, L. Y. Yang, W. J. Li, Y. Luo, J. N. Wang and R. J. Pei, *Chem. Sci.*, 2020, **11**, 6896-6906.
47. Y. Cheng, M. P. Cheng, J. Y. Hao, G. Q. Jia, D. Monchaud and C. Li, *Chem. Sci.*, 2020, **11**, 8846-8853.
48. J. Kosman, K. Zukowski and B. Juskowiak, *Molecules*, 2018, **23**, 1400.